# Plasma parameter investigation during plasma-enhanced chemical vapor deposition of silicon-containing diamond-like carbon films

T Grotjahn, Ö Aslanbas, M Mee, M König and S Meier
Fraunhofer Institute for Mechanics of Materials IWM,
79108 Freiburg, Germany

**Abstract**

In this work, tetramethylsilane-based PECVD processes were studied, and the deposited silicon-containing DLC films were analyzed. The main goal was to identify correlations between plasma parameters and the film structure and properties. The electron temperature, gas temperature, and hydrogen and silicon particle densities in these plasmas were calculated using optical emission spectroscopy measurements; the electron density and elastic electron collision rate were determined using self-excited electron resonance spectroscopy. The elemental composition of the films was determined by glow discharge optical emission spectroscopy, and the hardness and Young's modulus were characterized using nanoindentation. The plasma parameters of the gas temperature and electron temperature revealed stringent correlations with the film composition and properties and thus can already monitor the resulting properties during the deposition process. Increasing the gas temperature using power variation leads to reduced incorporation of silicon and hydrogen in the DLC films with a simultaneous increase of the film hardness. However, a gas temperature increase using a higher gas flow rate results in a decrease in the film hardness and an increase in the silicon and hydrogen contents. These results are promising concerning the use of plasma parameters for process control of CVD processes.

**Highlights**

- Plasma analysis by OES and SEERS of PECVD-based Si-DLC deposition processes
- Calculation of plasma particle densities, gas and electron temperature
- Si-DLC film characterization by nanoindentation, GDOES and Ramanspectroscopy
- Study of the effect of plasma parameters on film composition and properties
- Distinct dependency between hardness and gas and electron temperature

## 1. Introduction

Diamond-like carbon (DLC) films have attracted remarkable technological interest due to their unique combination of properties such as high hardness, low friction coefficient, high wear resistance, chemical inertness and high electrical resistivity [1–5]. Thus, these films are implemented in a wide range of applications, including magnetic storage disks [6], biomedical coatings [7–9], solar cells [10], automotive engineering [11] and, especially, tribological applications [2,4,12,13].

Considerable modifications of the mechanical and tribological properties as well as improved coating adhesion can be achieved by the incorporation of metallic and non-metallic elements. After the first investigations concerning metal incorporation [14,15], numerous additional

studies were performed. Ultra-hard Ti or W containing a-C:H films are used for cutting tools and automotive parts. Their specific properties are reported in [16–20]. Cr relaxes the internal stresses [21,22]. F-DLC has a strongly reduced surface energy [23] and is applied for biomedical applications, where the film reduces bacterial adhesion [24], prevents cell proliferation [25] and is considered as a material for blood-contacting devices [26]. N-DLC causes improved field emission [27,28], which makes this film attractive for field-emission display panels.

Silicon amorphous hydrogenated carbon coatings are of major interest and were extensively studied in the last decades because these materials can overcome several drawbacks of pure DLC. Si incorporation reduces residual internal stress [5,29–33] and improves film adhesion [34,35]. The coating hardness can be tailored to either increase [36,37] or decrease [31,38,39]. Tribological investigations revealed reduced friction coefficients [12,31,32,40,41] connected with better wear protection [33,40,42–44] and increased abrasive wear rates [23,31,39,41,45]. The thermal stability is improved [46,47], making these films interesting for a higher range of temperature. Furthermore, Si-DLC possesses reduced surface tension [23,48], corrosion resistance [49] and is blood- [50,51] and bio-compatible [52].

Further film modification and improvement can be achieved by the simultaneous incorporation of several elements such as Si-N-DLC [53–55] and Si-O-DLC [5,23,45,55], preparation of multilayer coatings [45,56,57] or surface texturing [58].

Numerous deposition techniques are applied for synthesizing DLC coatings [2–4,12], with plasma-enhanced chemical vapor deposition (PECVD) being the most preferred technique, which is able to coat even complex substrates at low temperatures. Thus far, tailoring the film properties was achieved empirically through the variation of process parameters, such as gas flow rates, generator power or process pressure. Nevertheless, the effect of the plasma condition on the deposition process and on coating properties is not yet fully understood. Thus, this paper concerns the correlation between the plasma state and film properties.

For plasma analysis, Langmuir probes are typically used, which have the disadvantage of creating local disruptions of the plasma. Mass spectroscopy is applied for the identification of chemical species in the plasma. The elastic electron collision rate as well as the electron density can be determined using self-excited electron resonance spectroscopy (SEERS) [59–61]. Optical emission spectroscopy (OES) also provides information about plasma species. Furthermore, based on the first approach of *actinometry* [62] to determine the absolute particle density by comparing the spectral line intensities of the investigated species with noble gas emission lines, several approaches to calculate the densities and electron temperature have been performed [63,64]. By simulating the emission band shapes of diatomic molecules, it is possible to determine the gas temperature [65–67].

Plasma diagnostic is frequently utilized in fundamental research for the calculation of plasma parameters of inert gas plasmas [66,68–70,63]. In addition, this technique is applied in deposition plasmas to investigate the effect of the plasma parameters on the film structure and properties [71–81]. By identifying the correlation, it should be possible to modify the film properties by adjusting the plasma parameters, and the transferability of coatings should thus be improved because the generation of comparable plasma conditions, especially particle energies and fluxes, should yield comparable resulting films [78]. For physical vapor deposition (PVD), in most cases, the film properties are correlated with the particle energies and fluxes. For CVD, the situation is more complicated because the generation of plasma is performed by the substrate electrode, which is not symmetrical in most cases. Hence, the distances between the substrate surface and the counter electrode (chamber wall) are changing. This fact leads to an inhomogeneous plasma distribution in the reaction chamber.

In the present work, argon-tetramethylsilane (TMS; SiC4H12) plasmas were used for Si-containing DLC film growth by PECVD. The film properties and composition were determined using nanoindentation, Raman and glow discharge optical emission spectroscopy (GDOES). The non-invasive plasma diagnostic methods of SEERS and OES were used to analyze the discharge conditions. By comparing emission line intensities, the absolute particle densities and energies were calculated with the aid of the *corona model* [64]. The gas flow rates and the generator power were varied to study their effects on the resulting discharge condition and coating properties. Correlations between the plasma parameters and film properties were investigated, and an approach for enhanced reproducibility was introduced.

## 2. Experimental Details

### *2.1. Chamber set-up and discharge conditions*

The schematic diagram in figure 1 illustrates the geometry and dimensions of the cylindrical deposition system. The aluminum chamber wall and the cover plate represent the grounded counter electrode. To prevent arcing during DLC film deposition, the inner chamber wall was lined with a 10-mm thick insulation sheet. This insulator interrupts the electric circuit between the matchbox, plasma and chamber wall, such that a DC bias measurement is not possible. The water-cooled radio frequency (RF) steel electrode (13.56 MHz) was located at the chamber bottom on the opposite of the gas inlet. The gas flow rates were adjusted using mass flow controllers. A rotary vane pump (Pfeiffer DUO 65C) and a turbo molecular pump (Leybold Turbovac 450) were used to pump the gas through the exhaust ring to create the process pressure. The OES adapter and the Hercules probe were mounted at a height of 40 mm above the substrate electrode.

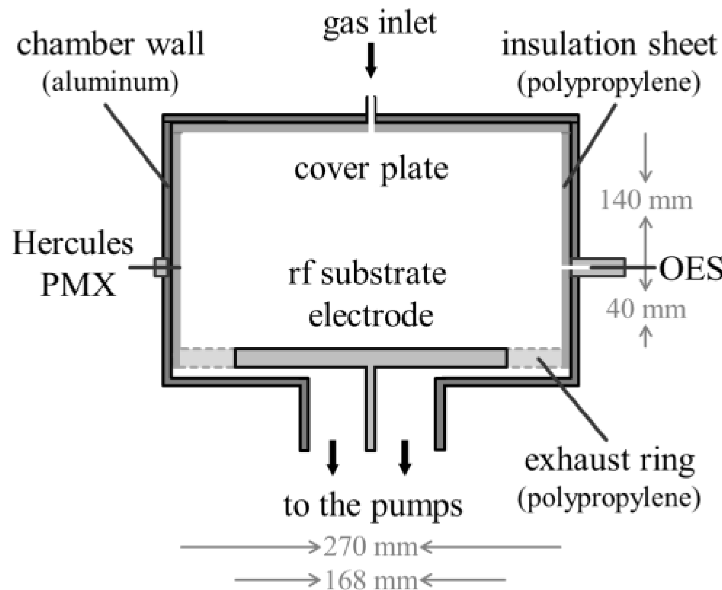


**Figure 1**: Scheme of the PECVD chamber with plasma monitoring instruments.

The films were deposited on flat steel rings (100Cr6; outer diameter = 35 mm, inner diameter = 20 mm, height = 2 mm), previously polished in multiple steps using diamond particle suspensions with particle sizes ranging from 15 µm to 3 µm. Substrate cleaning and activation were performed using argon plasma. For the film deposition process, argon and TMS with a fixed Ar:TMS gas flow ratio of 2.5 were used for all experiments. Furthermore, molecular nitrogen and neon were added for diagnostic purposes with a flow rate of approximately 5% of the flow rate of argon and TMS. During the deposition time, Si-DLC films of approximately 5-µm thickness were deposited.

The total gas flow rate and the generator output power were varied to investigate the effect of these parameters on the plasma parameters, film microstructure and mechanical properties. The correlation between the plasma parameters and the film properties was of particular importance. Two different total gas flow rates of 10.8 sccm (7.0 sccm argon, 2.8 sccm TMS, 0.5 sccm neon, 0.5 sccm nitrogen) and 24.6 sccm (16.0 sccm argon, 6.4 sccm TMS, 1.1 sccm neon, 1.1 sccm nitrogen) were used. Both these flow rates are commonly used for depositing films for industrial applications. The generator output power was varied from 100 W to 200 W in 20 W steps, which is the range in which films are producible with the used set-up.

### *2.2. Characterization of film structure and properties*

A portion of the substrate surface was covered during the deposition process to determine the coating thickness. The film thickness was measured using a profilometer (Hommel Tester T8000) by moving a diamond needle laterally across the step from the film to the covered area. The vertical position of the tip was recorded during these 4.8-mm line scans.

Surface roughness measurements were performed with an AFM (Veeco diDimension V). A cantilever with a spring constant of 40 N/m with a silicon tip was operated in tapping mode. The average surface roughness values were calculated from the height data using the built-in software of the AFM.

A nanoindenter (Fischerscope H100C XYp) equipped with a diamond pyramid (Vickers standard; face angle of 136°) was used to perform the indentation tests. The average surface roughness of all the deposited films fluctuated between 3 and 6 nm. Based on these results, reliable nanoindentation results are guaranteed with a penetration depth of 500 nm (approximately 10% of the film thickness). In total, 15 indentations per sample were performed with a loading and an unloading time of 30 s. By measuring the load force as a function of the penetration depth, the film hardness and Young’s modulus were calculated using the Oliver and Pharr method [82].

To determine the film composition, the coatings were analyzed using a glow discharge optical emission spectrometer (LECO GDS 850A). An RF source was used for plasma excitation and for removing the electrically isolating coating from the sample surface. To calculate quantitative mass information from the measured spectral intensities, four different Si-DLC coatings with known element distribution were used to define the calibration curves. The composition of these four coatings was determined at the Fraunhofer Institute for Surface Engineering and Thin Films using secondary ion mass spectrometry (SIMS). The carbon content of these films varied from 48 to 54 at.%, the silicon content varied from 21 to 24 at.% and the hydrogen content varied from 22 to 28 at.%. The calculation error for all the elements was approximately 0.5 at.%.

To verify the DLC phase formation, Raman spectra were measured using a Renishaw InVia spectrometer using a 20x objective lens and an excitation wavelength of 532 nm emitted from a Nd:YAG laser. To determine the peak characteristics, Gaussian profiles were fitted to the spectra.

### *2.3. Precursor particle densities*

To determine the electron temperature and plasma particle densities, the ratio of the precursor particle densities and the absolute densities of the noble gases were required. Using the measured chamber pressure and assuming a gas temperature of 300 K (room temperature), the ideal gas law predicts that for a total gas flow rate of 10.8 sccm and a pressure of 1 Pa and for a total gas flow rate of 24.6 sccm and a pressure of 2 Pa, the total neutral particle density before plasma ignition is approximately 2.4 $\times 10^{14}$ $cm^{-3}$ and 4.8 $\times 10^{14}$ $cm^{-3}$, respectively. The

most common method of determining the absolute noble gas densities and the ratio of the precursor particle densities is to calculate the percentage of the precursor gas flow rate from the total gas flow rate.

The rate at which molecules are transported out of the inner chamber is determined by the pumping speed, which depends on the intake pressure and the mass and atomic structure of the particles. Thus, every particle is pumped at a different rate. Therefore, the gas flow rate correction factors $CF$ must be assumed, which contain the characteristics of the set-up to determine more exact density values. The adjusted flow rate $f_X$ of the species $X$ is then given by a normalized flow rate $f_X' = f_X/CF$. The uncorrected case was compared with two other approaches. Welzel et al. presented a method for calculating correction factors based on pressure measurements [73] by recording the dependency of the gas flow rate on pressure for every precursor. Malyshev and Donnelly calculated correction factors based on their chamber set-up [83], discovering that "the effective pumping speed is approximately inversely proportional to the square root of mass" [63]. Table I presents the calculated densities for the three cases. During the deposition process, gas temperatures of approximately 350 K were measured for a total gas flow rate of 10.8 sccm. With respect to the calculated density value at 300 K, a temperature of 350 K reduces the value by approximately 14%.

**Table I:** Calculated precursor particle densities with and without correction techniques for the pumping power.

| | Unit | No correction | Pressure measurements correction | Mass correction |
|---|---|---|---|---|
| Ar density | $cm^{-3}$ | $1.6 \times 10^{14}$ | $1.4 \times 10^{14}$ | $1.4 \times 10^{14}$ |
| TMS density | $cm^{-3}$ | $6.3 \times 10^{13}$ | $9.2 \times 10^{13}$ | $8.4 \times 10^{13}$ |
| Ne density | $cm^{-3}$ | $1.1 \times 10^{13}$ | $8.3 \times 10^{12}$ | $8.3 \times 10^{12}$ |
| $N_2$ density | $cm^{-3}$ | $1.1 \times 10^{13}$ | $6.1 \times 10^{12}$ | $7.1 \times 10^{12}$ |

## 3. Plasma Parameter Determination

### *3.1. Self-excited electron resonance spectroscopy*

The plasma state was analyzed noninvasively by investigating the electron displacement current to the chamber wall using self-excited electron resonance spectroscopy (SEERS; Plasmetrex Hercules PMX). A physical model calculates the mean values of several process-relevant plasma parameters from the measurement signal, such as the electron density and elastic electron collision rate, in real time [59, 60, 61].

### *3.2. Optical Emission Spectroscopy*

In this work, a monochromator with a focal length of 750 mm (Princeton Instruments Arc SP2758) was used to investigate the plasma glow. Two gratings with different resolutions (1800 grooves $mm^{-1}$, wavelength region 200 – 1100 nm; 3600 grooves $mm^{-1}$, wavelength region 200 – 400 nm) were applied for diffraction. A CCD camera with 256 x 1024 pixels (PIXIS 256E) was used to measure the optical signal. The spectral sensitivity of the entire optical system was determined using an intensity-calibrated light source (Ocean Optics DH-2000) with a deuterium (wavelength region 220 – 400 nm) and halogen lamp (300 – 1050 nm). The calibration curves for each lamp were calculated.

Under deposition conditions, the recorded spectrum is dominated by strong argon spectral lines, especially in the range between 600 and 900 nm. Spectral lines of neon and hydrogen and a couple of emission bands of $N_2$ and $N_2^+$ exhibit sufficient intensity to be detectable. Furthermore, weak spectral lines of silicon and carbon appear in the region below 300 nm. The only detectable radical of TMS besides pure carbon and silicon is CH at 431.5 nm. Other $CH_x$ radicals possibly appearing in the discharge emit in the UV region below 200 nm and therefore cannot be detected by OES. To obtain information about these particles, other diagnostic techniques such as mass spectroscopy must be used. Every spectral line and band was measured several times with a shift of 3 pm of the captured wavelength region to obtain a more precise shape per line. Table II lists the investigated spectral lines and bands with their transitions and excitation energies.

**Table II:** Wavelengths, transition information and excitation energies from the ground states of investigated spectral lines and bands.

| Species | Wavelength in nm | Transition | | | $E_{Exc}$ in eV |
|---|---|---|---|---|---|
| Ne [a] | 585.249 | $2p_1$ | → | 1 s2 | 18.97 |
| Ar [a] | 750.387 | $2p_1$ | → | 1 s2 | 13.48 |
| Ar [a] | 751.465 | $2p_5$ | → | 1 s4 | 13.27 |
| Ar [a] | 794.818 | $2p_4$ | → | 1 s3 | 13.28 |
| Ar [a] | 800.616 | $2p_6$ | → | 1 s4 | 13.17 |
| Ar [a] | 811.531 | $2p_9$ | → | 1 s5 | 13.08 |
| Ar [a] | 842.465 | $2p_8$ | → | 1 s4 | 13.09 |
| Ar [a] | 852.144 | $2p_4$ | → | 1 s2 | 13.28 |
| H [b] | 434.047 | 5 | → | 2 | 13.06 |
| H [b] | 486.133 | 4 | → | 2 | 12.75 |
| H [b] | 656.279 | 3 | → | 2 | 12.09 |
| C | 247.856 | $3s\ ^1P^0$ | → | $2p^2\ ^1S$ | 7.68 |
| Si | 250.690 | $4s\ ^3P^0\ _{J=2}$ | → | $3p^2\ ^3P\ _{J=1}$ | 4.95 |
| Si | 251.432 | $4s\ ^3P^0\ _{J=1}$ | → | $3p^2\ ^3P\ _{J=0}$ | 4.93 |
| Si | 251.611 | $4s\ ^3P^0\ _{J=2}$ | → | $3p^2\ ^3P\ _{J=2}$ | 4.95 |
| Si | 251.920 | $4s\ ^3P^0\ _{J=1}$ | → | $3p^2\ ^3P\ _{J=1}$ | 4.93 |
| Si | 252.411 | $4s\ ^3P^0\ _{J=0}$ | → | $3p^2\ ^3P\ _{J=1}$ | 4.92 |
| Si | 252.851 | $4s\ ^3P^0\ _{J=1}$ | → | $3p^2\ ^3P\ _{J=2}$ | 4.93 |
| Si | 288.158 | $4s\ ^1P^0$ | → | $3p^2\ ^1D$ | 5.08 |
| CH | ~431 | $A^2\Delta\ _{v=0}$ | → | $X^2\Pi\ _{v=0}$ | 2.90 |
| $N_2$ | 380.490 | $C^3\ \Pi_{u\ v=0}$ | → | $B^3\ \Pi_{g\ v=2}$ | 11.05 |
| $N_2^+$ | 391.44 | $B^2\Sigma_u^+\ _{v=0}$ | → | $X^2\Sigma_g^+\ _{v=2}$ | 18.75 |

[a] Transition nomenclature: Paschen notation
[b] Transition nomenclature: main quantum number

### *3.2.1. Gas temperature*

By adding nitrogen to the plasma, the rotational temperature of molecular nitrogen can be determined by analyzing the shape of the vibrational $N_2$ or $N_2^+$ bands. For specific edge conditions, as preservation of the rotational distribution after electron collision excitation, the rotational temperature corresponds to the gas temperature. A detailed description of this method is given by Fantz [66, 84]. The gas temperature was calculated based on the $N_2$ $C^3\Pi_u$ – $B^3\Pi_g$ (ν= 0 – 2) and $N_2^+$ $B^2\Sigma_u^+$ – $X^2\Sigma_g^+$ (ν= 0 – 2) transitions. As argon is part of the discharge, the calculated rotational temperature from the $N_2$ transition may no longer

represent the gas temperature because of possible excitation transfer from metastable argon levels into the vibrational states of the $C^3\Pi_u$ state of nitrogen [85]. For this reason only, the $N_2^+$ transition reflects the gas temperature and can thus be used for calculation purposes.

### *3.2.2. Corona Model*

Due to the multiplicity and complexity of interactions within the plasma, sound assumptions and models are needed to describe the particle interactions during plasma deposition processes. For low-density and low-temperature plasmas, the dominant excitation and deexcitation processes can be described by the so-called *corona model* [64, 70, 86].

The electron energy distribution function (EEDF) is assumed to be Maxwellian, which is valid for an ionization degree of $10^{-4}$ [87]. Due to the excitation frequency and the inertia of ions, only the electrons have sufficient energy for the excitation of plasma particles. Furthermore, for low pressures (< 10 Pa), further population and depopulation processes, such as quenching or excitation by fragmentation, are negligible and the metastable densities of most species are too low to contribute to the excitation of higher electronic states [69, 70, 63, 88]. In particular, the hypothesis of negligible fragmentation excitation must be proven for each species. Under these assumptions, the rate balance equation for an excited state $l$ of a species $z$ is given by

$$n_0^z \cdot n_e \cdot k_{0,l}^z = n_l^z \cdot \Sigma_i \mathrm{A}_{l,i}, \qquad (1)$$

where $n_0^z$ and $n_l^z$ are the ground state and excited state densities of the species $z$, respectively, $n_e$ is the electron density, $A_{l,i}$ is the transition probability for spontaneous emission and $k_{0,l}^z$ is the rate coefficient from the ground state

$$k_{0,l}^z = \int_0^\infty \sigma_{0,l}^z(E_e) \cdot f(E_e) \cdot \sqrt{E_e}\, \mathrm{d}E_e, \qquad (2)$$

with the excitation cross section from the ground state $\sigma_{0,l}^z$ and the electron energy ($E_e$) depending on the Maxwellian EEDF $f$. The number of emitted photons per unit time is given by $\dot{N}_{l,m} = n_l^z \cdot \mathrm{A}_{l,m}$. The measured intensity $I_{l,m}^z$ depends on the spectral sensitivity of the system $\eta_{l,m}$ and on the detection volume $V$ and results in

$$I_{l,m}^z = n_0^z \cdot n_e \cdot \eta_{l,m}(\lambda) \cdot V \cdot \frac{A_{l,m}}{\Sigma_i \mathrm{A}_{l,i}} \cdot k_{0,l}^z. \qquad (3)$$

In the literature, sometimes instead of the cross sections and the rate coefficients, the emission cross sections $Q_{l,m}^z = A_{l,m}/\Sigma_i \mathrm{A}_{l,i} \cdot \sigma_{GS,l}^z$ or the emission rate coefficients $X_{l,m}^z = A_{l,m}/\Sigma_i \mathrm{A}_{l,i} \cdot k_{GS,l}^z$ are published. With a given electron density and using an absolutely calibrated spectrometer that provides the maximum spectral sensitivity, it is possible to determine the electron temperature directly from equation ( 3 ) by assuming the particle density of an inert gas [66].

### *3.2.3. Line ratio method*

If the spectroscopic system is not calibrated absolutely, as in the present case, one can use the line ratio method to calculate the electron temperature and the particle densities. Based on the emission rate coefficients, the intensity ratio of two spectral lines is given by

$$\frac{I_{l,m}^z}{I_{l,m}^y} = \frac{n_{GS}^z}{n_{GS}^y} \cdot \frac{\eta_{l,m}^z}{\eta_{l,m}^y} \cdot \frac{X_{l,m}^z(T_e)}{X_{l,m}^y(T_e)}. \qquad (4)$$

The emission rate coefficient is a function of the electron temperature $T_e$. If the particle density ratio are known, the electron temperature can be calculated. Analogously, if the

electron temperature and one particle density is known, it is possible to calculate the other particle density.

### *3.2.4. Electron temperature*

The electron temperature can be calculated by comparing the neon spectral line of 585.249 nm with the recorded argon lines (see table II). This process is justified by the fact that the particle densities of inert gases, which are calculated from the gas flow rates, should be approximately the same under the used plasma conditions due to the small ionization and excitation rates and the low fragmentation probability. The apparent cross-sections reported by Chilton et al. for argon [89] and neon [90] were used to determine the emission rate coefficients and the following evaluations. Fuhr et al. list the transition probabilities for spontaneous emission [91].

### *3.2.5. Particle densities*

After evaluation of the electron temperature, the densities of emitting fragment species are calculated by comparing their spectral lines with the lines of argon and neon. The absolute argon and neon particle densities were estimated as described in section 2.3. Three strong atomic hydrogen lines were detected. The emission rate coefficients for direct excitation, published by Behringer and Fantz [92], were used for the density calculation of the atomic hydrogen. The effect of dissociation was estimated for the excitation from TMS to the hydrogen level n = 4. The latter represents the excited state that generates the $H_\beta$ spectral line at 486.133 nm. Kurunczi et al. published the dissociation rate coefficient for this transition [93]. In all the experiments, the hydrogen density caused by dissociation excitation was always smaller than 0.7% of the hydrogen density caused by ground state excitation. Assuming that the dissociation rate coefficients into the other both excited hydrogen states are of the same order of magnitude, the dissociation excitation from TMS to hydrogen is negligible. Furthermore, because the density of hydrogen containing TMS fragments is lower than the TMS density before plasma ignition, the dissociation excitation out of these levels can also be neglected.

As described in section 3.2.1, several atomic silicon spectral lines were detected (Table II). Silicon consists of an electronic ground state ($3p^2\ ^3P$) in the triplet system and two low-energetic metastable states in the singlet system ($3p^2\ ^1S$, $3p^2\ ^1D$) with a slightly higher energy than the $3p^2\ ^3P$ state. Particles can also accumulate in both of these singlet system states. For an exact calculation of the silicon particle density, the particle densities of all of these three states must be calculated, which is not possible in the present case because of the weak spectral line emission intensities of the $4\ s\ ^1P^0$ - $3p^2\ ^1S$ and the $4\ s\ ^1P^0$ - $3p^2\ ^1D$ transitions. However, it is possible to calculate the silicon ground state density. Fantz published the rate coefficients for the electron impact excitation from the ground state ($3p^2\ ^3P$) to the $4\ s\ ^3P^0$ state [84]. With the transition probability values from Fuhr et al. [91], the resulting silicon ground state particle densities for the six lines were calculated. Five densities are in very good agreement with each other. Only the calculated density from the 252.411 nm line exhibits an aberration. This effect cannot be explained accurately. It is supposed that there is a correlation with the non-existing $4\ s\ ^3P^0\ _{J=0} \rightarrow 3p^2\ ^3P\ _{J=0}$ transition, which should result from the same excited level as the 252.411 nm line. Because of this aberration, the mean value of the five other densities was used for further analysis. Due to the particle accumulation in the metastable states of the singlet system, the real silicon particle density in the plasma is higher than the calculated value. Fantz reported that for a silane ($SiH_4$)-based plasma, 20% of the silicon particles accumulated in the $3p^2\ ^1D$ state and 5% accumulated in the $3p^2\ ^1S$ state [84].

## 4. Results and Discussion

### *4.1.Hydrogen and silicon particle densities*

The atomic hydrogen and silicon particle densities that result from the different spectral lines were calculated and compared with information about their agreement. These calculations were performed for a total gas flow rate of 10.8 sccm with a generator output power of 200 W and without pumping speed correction. In this case, the calculated mean electron temperature of all the argon-neon spectral line combinations was 5.7 ± 0.4 eV. For each of the three hydrogen spectral lines of the Balmer series and for five of the six silicon lines of the 4 s $^3P^0 \rightarrow 3p^2\ ^3P$ transition, the silicon particle density was calculated two times, first, by comparison with the neon line and, second, by calculating the mean particle density, which results from the density values from the comparison with the nine argon lines.

*Hydrogen:* Taking only the neon spectral line for the hydrogen particle density calculation, the density increases from 3.1 $x10^{12}$ $cm^{-3}$ for the 434.047 nm line to 3.3 $x10^{12}$ $cm^{-3}$ for the 486.133 nm and to 3.7 $x10^{12}$ $cm^{-3}$ for the 656.279 nm line with a mean value of 3.3 $x10^{12}$ $cm^{-3}$. The mean hydrogen particle density, which results from comparison with the argon lines, increases in the same order from 3.0 $x10^{12}$ $cm^{-3}$ to 3.3 $x10^{12}$ $cm^{-3}$ to 3.6 $x10^{12}$ $cm^{-3}$ with the same average of 3.3 $x10^{12}$ $cm^{-3}$. The calculation error for all the densities is approximately 15%.

*Silicon:* The same procedure was applied for the five spectral lines of the triplet system. The calculated densities for the five spectral lines for both cases, compared with argon and neon, were in good agreement. The mean density obtained by the lines of neon and argon were 7.8 $x10^9$ $cm^{-3}$ and 7.7 $x10^9$ $cm^{-3}$, respectively.

For time-resolved plasma state characterization, the number of monitored spectral lines must be reduced due to the required high exposure times. According to our results, reliable particle density values can also be obtained after decreasing the number of observed spectral lines. Capturing the Ne 585.249 nm line, the Ar 750.387 nm and the Ar 751.45 nm lines are sufficient for electron temperature and density calculations. Furthermore, it is recommended to monitor the $H_\beta$ line because this particle density value agrees with the mean density value. The wavelengths of the silicon spectral lines are similar enough to each other that the spectral lines can be captured in a single measurement.

### *4.2.Effect of gas flow rate correction factors*

The effect of the gas flow rate correction factors, which were introduced in section 2.3, related to the electron temperature and particle densities of hydrogen as well as silicon was analyzed using the three particle density calculation techniques. These calculations were performed for a total gas flow rate of 10.8 sccm and with a generator output power of 200 W.

Without any correction of the pumping rate, the electron temperature was 5.7 ± 0.4 eV. The hydrogen density was 3.3 $x10^{12}$ $cm^{-3}$, the silicon density was 7.8 $x10^9$ $cm^{-3}$ and 7.7 $x10^9$ $cm^{-3}$ when using argon spectral lines for the calculation. The error of the determined densities was approximately 15%. Using the flow rate correction approaches for determining the plasma parameters, the calculated electron temperature and the particle densities varied. However, the calculated values using the two correction techniques did not differ significantly from each other, although the pressure measurement correction approach includes the used chamber set-up and pumping characteristics, and the mass-based correction approach is based on the chamber of Malyshev and Donnelly [83].

For both correction techniques, the electron temperature was approximately 2 eV higher than that without the pumping speed correction. Furthermore, the hydrogen particle density values were slightly increased (3.5 to 3.6 $x10^{12}$ $cm^{-3}$) and the silicon densities were 20-25% higher

(9.3 to 9.8 x$10^9$ $cm^{-3}$). These results are presented in table III. It can be deduced that the electron temperature has a weak effect on the calculated hydrogen density but a much larger effect on the silicon density. An explanation for this effect might be the different excitation threshold energies of hydrogen (12.75 eV) and silicon (4.92 – 4.95 eV). A change of the electron temperature mainly affects the shape of the EEDF in the low-energy region. The number of high-energetic electrons is less affected. Another correction of the neon to argon ratio would shift the absolute temperature and particle density values but does not affect the behavior of the electron temperature and the calculated densities under the changed process conditions. In additional experiments, it was confirmed that the results are reproducible within a deviation of less than 5%. Based on these results, the pressure measurement correction approach was used for further plasma parameter calculations, and only one electron temperature and density for each species was used, which was the average value of several spectral line calculations.

**Table III:** Effect of the pumping power correction approaches on electron temperature and particle densities and dependency on the species used for calculation.

| | Unit | No correction | | Pressure measurements correction | | Mass correction | |
|---|---|---|---|---|---|---|---|
| | | Ne | Ar | Ne | Ar | Ne | Ar |
| Electron temperature | eV | 5.7 ± 0.4 | | 7.7 ± 0.6 | | 7.5 ± 0.5 | |
| Mean H density | $cm^{-3}$ | 3.3 x $10^{12}$ | 3.3 x $10^{12}$ | 3.6 x $10^{12}$ | 3.5 x $10^{12}$ | 3.5 x $10^{12}$ | 3.5 x $10^{12}$ |
| Mean Si density | $cm^{-3}$ | 7.8 x $10^9$ | 7.7 x $10^9$ | 9.8 x $10^9$ | 9.6 x $10^9$ | 9.5 x $10^9$ | 9.3 x $10^9$ |

*4.3. Effect of process parameter variation*

The effect of the gas flow rate and generator power on plasma parameters and film properties was studied. As mentioned in section 2.1, two different total gas flow rates of 10.8 and 24.6 sccm were used, and the generator output power was varied from 100 to 200 W. Due to the impossibility of measuring the bias voltage, additional experiments without the insulator were performed to obtain information about the bias voltage. Using the same gas flow rates and generator powers, the bias voltage was determined to be in the range from 350 V to 500 V.

In figure 2, the effect of the generator power and gas flow rate variation on the gas and electron temperature is demonstrated. A higher generator power leads to an increase of the gas temperature due to an increased energy transfer into the plasma. For a total flow rate of 10.8 sccm and 24.6 sccm, the gas temperature value increased from 348 to 367 K and from 365 to 396 K, respectively. The increase of the gas temperature for a higher gas flow rate can be explained by the higher collision rate in the sheath between accelerated ions and neutrals, which causes neutral gas heating.

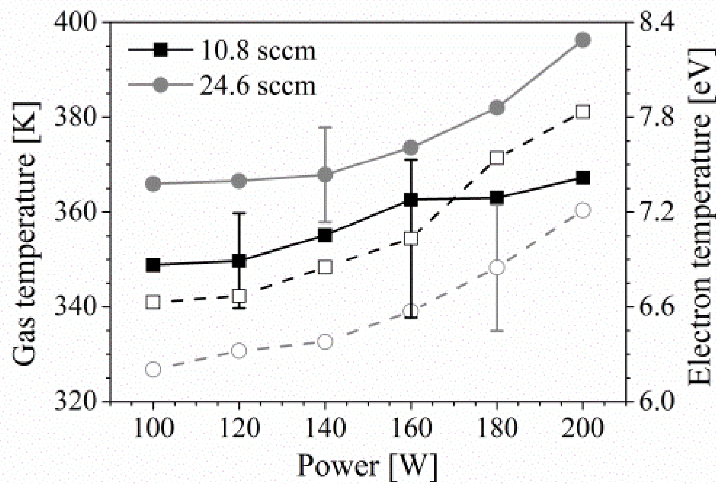


**Figure 2**: Effect of the process parameter variation on gas temperature (filled symbols) and electron temperature (empty symbols).

The electron temperature also increases with the generator power, from 6.6 to 7.8 eV for a flow rate of 10.8 sccm and from 6.2 to 7.2 eV for 24.6 sccm. The temperature decrease for the higher flow rate is presumably conditioned by the shorter mean free path of electrons. Consequently, the electrons dispense their gained energy faster and more frequently through inelastic collisions.

Figure 3 depicts the effect of the process parameter variation related to the electron density and elastic electron collision rate. For both flow rates, the elastic collision rate does not exhibit continuous behavior during power variation. Using the lower total flow rate, the collision rate increases from 100 to 160 W from 5.1 to 5.7 x$10^7$ 1/s before decreasing to 5.2 x$10^7$ 1/s at 200 W. With a gas flow rate of 24.6 sccm, the same behavior is observed, with an increase from 5.8 to 6.5 x$10^7$ 1/s before a reduction to 6.2 x$10^7$ 1/s. The increase of the collision rate with a higher flow rate can again be explained by the shorter mean free path. The elastic collision rate behavior during generator power variation can be explained by its factors of influence, such as the collision cross-section, the EEDF and the particle neutral density, which under the assumption of the ideal gas law is indirectly proportional to the gas

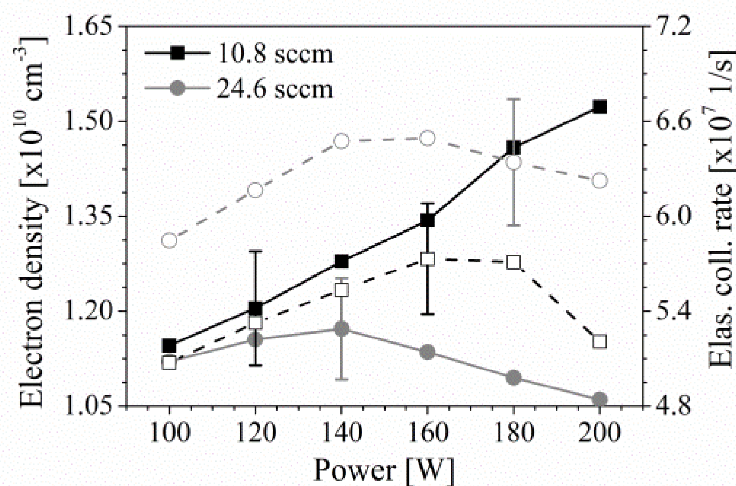


**Figure 3**: Effect of process parameters on electron density (filled symbols) and elastic collision rate (empty symbols).

temperature. Thus, depending on which effect dominates, the elastic collision rate increases or decreases. It is also possible to calculate the neutral density to determine the course of the EEDF; however, a description of the cross-section for elastic collision and, therefore, a statement concerning the collision rate behavior are complicated. A combination of these effects might be the reason for the behavior of the electron density, which is also illustrated in figure 3: while increasing steadily for a flow rate of 10.8 sccm from 1.15 to 1.52 $x10^{10}$ $cm^{-3}$, the electron density shifts between 1.06 and 1.17 $x10^{10}$ $cm^{-3}$ for 24.6 sccm.

The calculated hydrogen and silicon particle densities confirm the expectations. The increase of the generator power forces TMS fragmentation and leads to a higher particle density. For a total flow rate of 10.8 sccm, the hydrogen particle density increases from approximately 3.3 to 7.6 $x10^{12}$ $cm^{-3}$, and the silicon density increases from 1.4 to 3.6 $x10^{9}$ $cm^{-3}$. With the addition of precursor molecules to the discharge, more H and Si particles are formed. A higher gas flow rate creates approximately twice as much hydrogen (7.3 $x10^{12}$ to 1.4 $x10^{13}$ $cm^{-3}$) and a three times higher silicon density (4.4 to 9.8 $x10^{9}$ $cm^{-3}$). A higher hydrogen particle density suggests a decreased amount of hydrogen in the hydrocarbon and organosilicon species; in addition, a higher silicon particle density indicates less silicon-containing TMS fragments. These molecules are assumed to be the responsible species for the deposition process and for the incorporated silicon amount in DLC films [73, 74].

The effects of the varied generator power and gas flow rates on the hardness and Young's modulus are demonstrated in figure 4. For a total gas flow rate of 10.8 sccm, the film hardness increases from 11.8 to 18.1 GPa if the generator power increases; for a flow rate of 24.6 sccm, the hardness increases from 10.5 to 16.1 GPa. The Young's modulus exhibits the same behavior, increasing from 102 to 152 GPa for a flow rate of 10.8 sccm and from 93 to 138 GPa for a flow rate of 24.6 sccm.

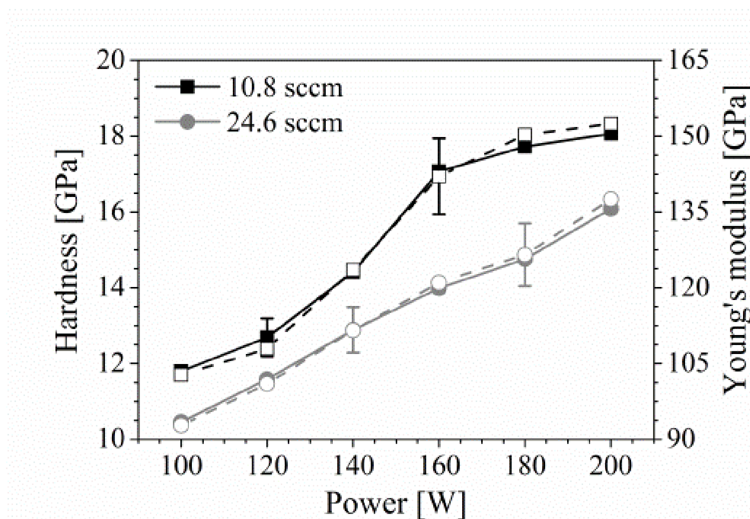


**Figure 4**: Layer hardness (filled symbols) and Young's modulus (empty symbols) as a function of the generator output power for the flow rates of 10.8 sccm (squares) and 24.6 sccm (circles).

Table IV lists the hardness and Young's modulus values as well as the film composition of the deposited films. Only small changes in the compositions were detected. An increase of the generator power implies less silicon and hydrogen incorporation. For the lower total gas flow rate, the hydrogen content decreased from 25.5 to 23.3 at.% and the silicon content decreased from 24.0 to 22.6 at.%, while the carbon content increased from 50.4 to 53.5 at.%. For a flow rate of 24.6 sccm, the changes were on the same order of magnitude. The hydrogen content decreased from 26.0 to 25.0 at.%, the silicon content decreased from 24.6 to 23.4 at.% and the carbon content increased from 49.2 to 51.2 at.%. Due to the combination of the composition

determination method of the calibration standards and the GDOES calibration and measurement, an error of approximately 1 at.% is assumed for the calculated composition values. Thus, the variations in the compositions could be due to measurement uncertainty. Nevertheless, a continuous change is observed, in combination with a change of the plasma state and of the macroscopic film properties; thus, an altered coating composition can be expected. By increasing the generator power, the decrease in the silicon content in the films agrees with the statement of less silicon-containing $Si(C_yH_x)$ fragments in the plasma.

**Table IV:** Film composition, hardness, Young's modulus and peak position of Raman spectra of Si-DLC coatings. Missing values of composition to 100 at.%: nitrogen, argon, neon.

| total flow rate sccm | generator power W | C at.% | H at.% | Si at.% | hardness GPa | Young's modulus GPa | peak position $cm^{-1}$ |
|---|---|---|---|---|---|---|---|
| 10.8 | 100 | 50.4 | 25.4 | 24.0 | 11.8 | 102.8 | 1443.4 |
| | 120 | 50.7 | 25.2 | 23.8 | 12.7 | 107.9 | 1451.3 |
| | 140 | 51.5 | 25.0 | 23.1 | 14.4 | 123.5 | 1456.8 |
| | 160 | 52.0 | 24.8 | 22.8 | 17.1 | 142.0 | 1458.8 |
| | 180 | 52.8 | 24.0 | 22.7 | 17.7 | 150.3 | 1459.8 |
| | 200 | 53.3 | 23.3 | 22.6 | 18.1 | 152.4 | 1460.6 |
| 24.6 | 100 | 49.2 | 26.0 | 24.6 | 10.5 | 92.8 | 1447.9 |
| | 120 | 49.3 | 25.8 | 24.5 | 11.6 | 101.0 | 1450.1 |
| | 140 | 50.0 | 25.6 | 24.3 | 12.9 | 111.6 | 1452.3 |
| | 160 | 50.1 | 25.5 | 24.1 | 14.0 | 121.0 | 1456.0 |
| | 180 | 51.0 | 25.1 | 23.4 | 14.8 | 126.5 | 1457.1 |
| | 200 | 51.2 | 25.0 | 23.4 | 16.1 | 137.5 | 1457.9 |

Additionally, the films were analyzed by Raman spectroscopy to analyze the DLC phase formation. The Raman spectra of the pure DLC films exhibit a broad asymmetric signal, which is a superposition of the strong G mode of graphite near 1543 $cm^{-1}$ (stretching motion of $sp^2$ bonded C=C pairs) and the weaker D peak near 1355 $cm^{-1}$, whose intensity is strictly connected with the breathing motion of six-fold aromatic rings [94]. For the presented coatings, instead of two peaks, only a broad band with a maximum in the range from 1443 to 1461 $cm^{-1}$ is observed. Figure 5 presents the spectra for different generator powers and a constant total gas flow rate of 10.8 sccm. In figure 6, the spectra for the same generator powers but a higher flow rate are presented. With increasing Si content, a shift of the G peak to lower wavenumbers as well as a decrease of the D peak, disappearing at approximately 20 at.% Si, was observed by other authors [5, 53, 49, 95]. The disruption of the six-fold aromatic rings by silicon incorporation is the reason for this effect [94]. The films of the present study reveal an even stronger peak shift than in the cited references, which could indicate a higher proportion of silicon than 20 at.%. This result would also confirm the measured silicon concentrations of the coatings as well as their change. Despite the small composition changes during the power variation, for both flow rates, the peak position moves to lower wavenumbers with increasing silicon content.

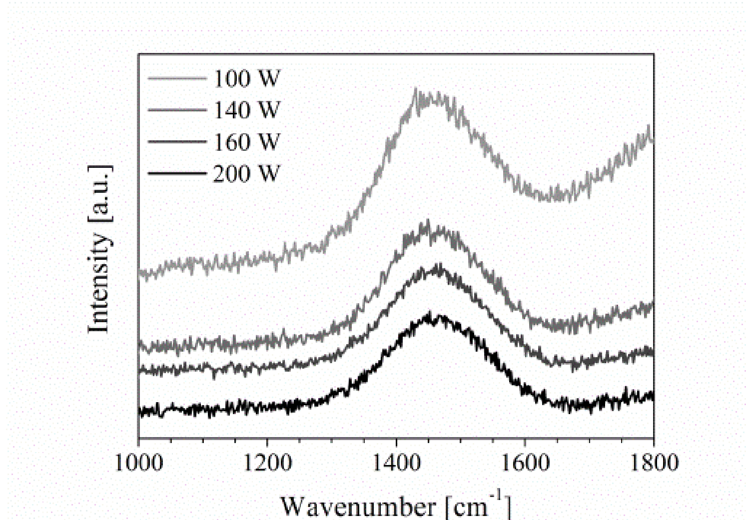


**Figure 5**: Raman spectra of deposited films for various generator powers and a total gas flow rate of 10.8 sccm.

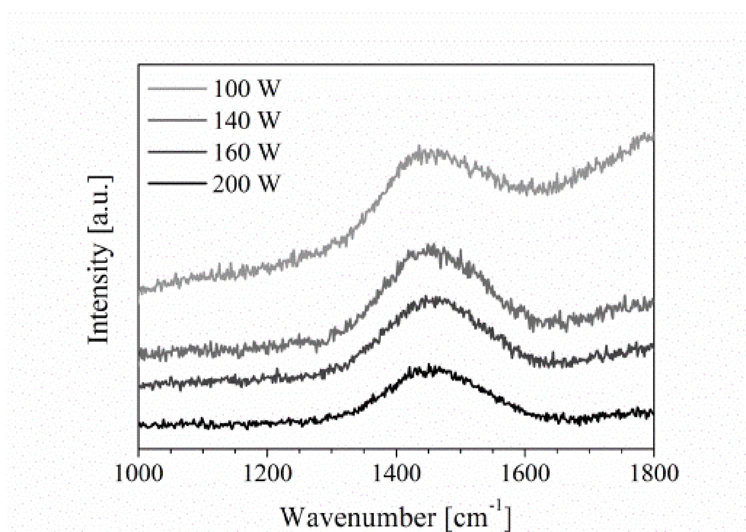


**Figure 6**: Raman spectra of deposited films for various generator powers and a total gas flow rate of 24.6 sccm.

All the results of the film analysis measurements agree regarding the change of film properties under process parameter variation. Furthermore, a change in one property always implies a change in other properties. For the presented films, a higher carbon content implies less silicon and hydrogen in the coatings and an increase of hardness and Young's modulus. In addition, the ratio of the hardness to the Young's modulus remains approximately constant.

### *4.4. Correlation between plasma parameters and film properties*

The effect of the plasma parameters on the film composition and macroscopic properties was studied. Exemplary for the structural and mechanical properties, the hardness was used due to the mentioned interdependency between the film properties.

The effects of the gas and electron temperature on the hardness are demonstrated in figure 7. The dependencies exhibit continuous behavior. An increase of the gas or electron temperature generates a harder coating. However, depending on the adjusted flow rate, other gas temperature and electron temperature values are required for the same film hardness. Figure 8

depicts the correlation of the elastic electron collision rate and the electron density with the coating hardness. The interpretation is difficult because, for example, the same collision rate values can lead to different hardness values. For the electron density, no continuous dependency is evident. In summary, for the present case, there is no possibility of assigning an electron density or a collision rate value to a specific hardness value.

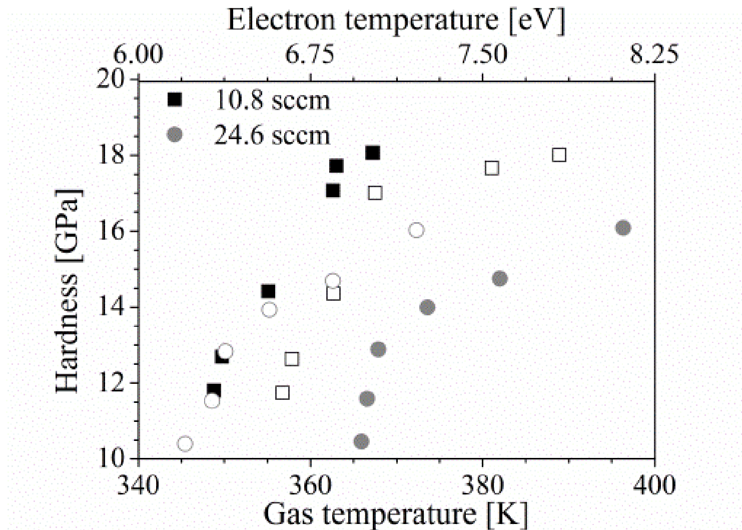


**Figure 7**: Effect of gas temperature (bottom abscissas, filled symbols) and electron temperature (top abscissas, empty symbols) on layer hardness and dependency on the flow rates of 10.8 sccm (squares) and 24.6 sccm (circles).

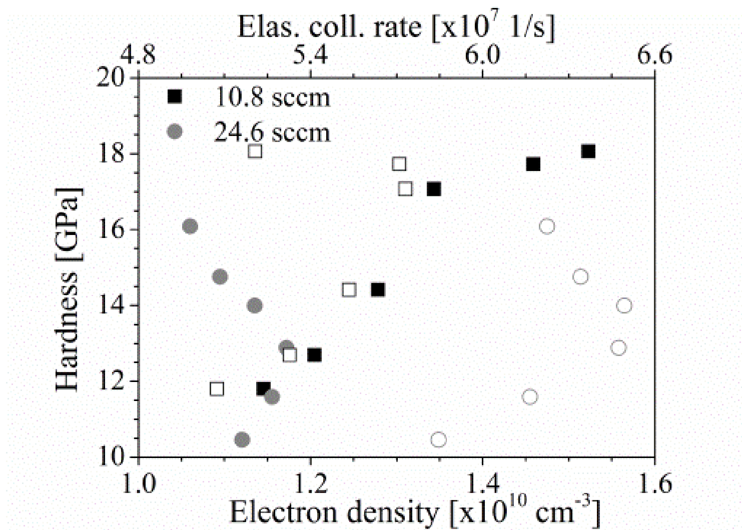


**Figure 8**: Effect of electron density (bottom abscissas, filled symbols) and elastic collision rate (top abscissas, empty symbols) on layer hardness and dependency on the flow rates of 10.8 sccm (squares) and 24.6 sccm (circles).

### *4.5.Enhanced reproducibility and process control*

As described by other authors [73, 74, 78], the identification of correlations between plasma parameters, especially densities and energies, and film characteristics is the key for enhanced process reproducibility, transferability and for a better understanding of the deposition process. Comparable plasma conditions should yield similar film properties. To achieve this goal, plasma parameters that exhibit distinct and continuous dependencies on the film structure and properties for a determined modification of coatings, enhanced reproducibility and process control are required. It is obvious that several plasma parameters must be

observed, and their mutual-dependencies must be known. With respect to the presented results, the elastic collision rate and electron density are not recommended for process control. In contrast, the gas temperature and electron temperature exhibit the required distinct behavior and, therefore, can be used.

The use of plasma parameters for process control also implies other benefits. An adjustment can be performed by the variation of the flow rates, by changing the generator power or even by mismatching. Thus, the process no longer depends on the generator output power. The generator output power is a problematic parameter for process control because even at a fixed power value, a varying amount of energy could be transferred into the plasma due to thermal and contact losses in the matchbox, which in turn would lead to different film properties. This technique demonstrates an initial simple approach to improve process reproducibility. Before implementing the method in practical applications, further studies considering a broader range of values, such as an investigation of the effect of substrate geometry or variation of the argon to TMS gas flow ratio should be performed.

## 5. Conclusions

PECVD processes of silicon containing DLC films were investigated using OES and SEERS. The film properties and elemental compositions were determined using indentation measurements, Raman and GDOES.

The first objective of this work was to establish a plasma analysis technique under deposition conditions for the reliable determination of absolute plasma parameter values, especially concerning the parameters that are calculated from spectral lines. The second objective was to improve the understanding of the effect of plasma parameters on film properties, which is required for improved process reproducibility, film optimization or interpretation of the deposition mechanism.

Based on the plasma emission, the gas temperature, electron temperature and particle densities of atomic hydrogen and silicon were determined. These parameters were evaluated using different combinations of spectral lines and lead to the same parameter values. Hence, the quantity of the spectral lines that must be captured to achieve reliable values could be reduced. Furthermore, different approaches for the calculation of the noble gas densities were compared.

In contrast to the electron density and the electron collision rate, the gas and electron temperatures revealed distinct behavior under process parameter variation.

Within the investigated parameter range, a higher generator power and a lower total gas flow rate lead to an increase of hardness and Young's modulus in addition to a reduced silicon content in the films.

Using plasma parameters for process control, an increase in process reproducibility can be expected. Based on the results of the presented case, the gas temperature and the electron temperature are suitable for process control, as these parameters have a distinct dependency on the film properties. However, for a reliable control, further extensive studies, including further parameter variations and discussions concerning particle energies and densities are necessary.

## Acknowledgments

This research and development project was funded by the German Federal Ministry of Education and Research (BMBF) within the Framework Concept "Research for Tomorrow's

Production" (funding number 02PO2421) and was managed by the Project Management Agency Karlsruhe (PTKA). The authors are responsible for the contents of this publication.

The authors gratefully acknowledge Prof. Karsten Durst and Christoph Schmid from the Department of Materials Science and Engineering of the University of Erlangen-Nuremberg for their valuable suggestions within the German Research Foundation (DFG) project DU-424/7-1.

## References

[1] K. Oguri, T. Arai, Surf. Coat. Technol. 47 (1991) 710-721.

[2] A. Grill, Surf. Coat. Technol. 94-95 (1997) 507-513.

[3] J. Robertson, Mater. Sci. Eng. R Rep 37 (2002) 129-281.

[4] A. Erdemir, C. Donnet, J. Phys. D: Appl. Phys. 39 (2006) 311-327.

[5] C. Chouquet, G. Gerbaud, M. Bardet, S. Barrat, A. Billard, F. Sanchette, C. Ducros, Surf. Coat. Technol. 204 (2010) 1339-1346.

[6] P.R. Goglia, J. Berkowitz, J. Hoehn, A. Xidis, L. Stover, Diamond Relat. Mater. 10 (2001) 271-277.

[7] R. Hauert, Tribol. Int. 37 (2004) 991-1003.

[8] J. Endrino, R.E. Galindo, H.S. Zhang, M. Allen, R. Gago, A. Espinosa, A. Anders, Surf. Coat. Technol. 202 (2008) 3675-3682.

[9] G. Dearnaley, J.H. Arps, Surf. Coat. Technol. 200 (2005) 2518-2524.

[10] S. Tinchev, P. Nikolova, S. Balabanov, N. Georgiev, J Phys. Conf. Ser. 113 (2008) 012026.

[11] M. Kano, New Diamond Front. Carbon Technol. 16 (2006) 201-210.

[12] C. Donnet, Surf. Coat. Technol. 100 (1998) 180-186.

[13] A. Grill, Diamond Relat. Mater. 8 (1999) 428-434.

[14] H. Dimigen, H. Hübsch, R. Memming, Appl. Phys. Lett. 50 (1987) 1056-1058.

[15] H. Dimigen, C.P. Klages, Surf. Coat. Technol. 49 (1991) 543-547.

[16] K. Bewilogua, C.V. Cooper, C. Specht, J. Schröder, R. Wittorf, M. Grischke, Surf, Coat. Technol. 132 (2000) 275-283.

[17] C. Strondl, N.M. Carvalho, J.T.M. DeHosson, G.J. Kolk, Surf. Coat. Technol. 162 (2003) 288-293.

[18] W. Precht, A. Czyzniewski, Surf. Coat. Technol. 174 (2003) 979-983.

[19] A. Czyzniewski, W. Precht, J. Mater. Process. Technol. 157-158 (2004) 274-283.

[20] J. Güttler, J. Reschke, Surf. Coat. Technol. 60 (1993) 531-535.

[21] V. Singh, J.C. Jiang, E.I. Meletis, Thin Solid Films 489 (2005) 150-158.

[22] A. Pardo, C. Gomez-Aleixandre, J. Orwa, A. Cimmino, S. Prawer, Diamond Relat. Mater. 26 (2012) 39-44.

[23] M. Grischke, A. Hieke, F. Morgenweck, H. Dimigen, Diamond Relat. Mater. 7 (1998) 454-458.

[24] M. Ishihara, T. Kosaka, T. Nakamura, K. Tsugawa, M. Hasegawa, F. Kokai, Y. Koga, Diamond Relat. Mater. 15 (2006) 1011-1014.

[25] R. Hauert, U. Müller, G. Francz, F. Birchler, A. Schroeder, J. Mayer, E. Wintermantel, Thin Solid Films 308 (1997) 191-194.

[26] T. Saito, T. Hasebe, S. Yohena, Y. Matsuoka, A. Kamijo, K. Takahashi, T. Suzuki, Diamond Relat. Mater. 14 (2005) 1116-1119.

[27] K.R. Lee, K.Y. Eun, S. Lee, D.R. Jeon, Thin Solid Films 290 (1996) 171-175.

[28] N. Dwivedi, S. Kumar, R.K. Tripathi, H.K. Malik, O.S. Panwar, Appl. Phys. A 105 (2011) 417-425.

[29] J.C. Damasceno, S.S. Camargo Jr, M. Cremona, Thin Solid Films 420 (200) 195-199.

[30] M. Ban, M. Ryoji, S. Fujii, J. Fujioka, Wear 253 (2002) 331-338.

[31] M. Ikeyama, S. Nakao, Y. Miyagawa, S. Miyagawa, Surf. Coat. Technol. 191 (2005) 38-42.

[32] K. Baba, R. Hatada, S. Flege, W. Ensinger, Surf. Coat. Technol. 203 (2009) 2747-2750.

[33] A. Gangopadhyay, P. Willermet, M. Tamor, W. Vassell, Tribol. Int. 30 (1997) 9-18.

[34] D. Neerinck, P. Persoone, M. Sercu, A. Goel, D. Kester, D. Bray, Diamond Relat. Mater. 7 (1998) 468-471.

[35] W.J. Wu, M.H. Hon, Thin Solid Films 345 (1999) 200-207.

[36] K.R. Lee, M.G. Kim, S.J. Cho, K.Y. Eun, T.Y. Seong, Thin Solid Films 308-309 (1997) 263-267.

[37] J. Meneve, E. Dekempeneer, J. Smeets, Diamond Films Technol. 4 (1994) 23-36.

[38] J.F. Zhao, P. Lemoine, Z.H. Liu, J.P. Quinn, P. Maguire, J.A. McLaughlin, Diamond Relat. Mater. 10 (2001) 1070-1075.

[39] H. Nakazawa, Y. Asai, T. Kinoshita, M. Suemitsu, T. Abe, K. Yasui, T. Itoh, T. Endoh, Y. Narita, A. Konno, Y. Enta, M. Mashita, Jpn. J. Appl. Phys. 47 (2008) 8491-8497.

[40] R. Gilmore, R. Hauert, Thin Solid Films 398 (2001) 199-204.

[41] D. Hofmann, S. Kunkel, K. Bewilogua, R. Wittorf, Surf. Coat. Technol. 215 (2012) 357-363.

[42] S.J. Park, K.R. Lee, D.H. Ko, Tribol. Int. 37 (2004) 913-921.

[43] A. Varma, V. Palshin, E.I. Meletis, Surf. Coat. Technol. 148 (2001) 305-314.

[44] O.K. Porada, V.I. Ivashchenko, L.A. Ivashchenko, G.V. Rusakov, S.N. Dub, A.I. Stegnij, Surf. Coat. Technol. 180 (2004) 122-126.

[45] K. Bewilogua, I. Bialuch, H. Ruske, K. Weigel, Surf. Coat. Technol. 206 (2011) 623-629.

[46] S.S. Camargo Jr, R.A. Santos, A.B. Neto, R. Carius, F. Finger, Thin Solid Films 332 (1998) 130-135.

[47] W.J. Wu, M.H. Hon, Surf. Coat. Technol. 111 (1999) 134-140.

[48] L.Y. Chen, F.C.N. Hong, Diamond Relat. Mater. 12 (2003) 968-973.

[49] P. Papakonstantinou, J.F. Zhao, P. Lemoine, E.T. McAdams, J.A. McLaughlin, Diamond Relat. Mater. 11 (2002) 1074-1080.

[50] T.I.T. Okpalugo, A.A. Ogwu, P.D. Maguire, J.A.D. McLaughlin, D.G. Hirst, Diamond Relat. Mater. 13 (2004) 1088-1092.

[51] T.I.T. Okpalugo, A.A. Ogwu, P.D. Maguire, J.A.D. McLaughlin, Biomater. 25 (2004) 239-245.

[52] T.I.T. Okpalugo, A.A. Ogwu, P.D. Maguire, J.A.D. McLaughlin, Technol. Health Care 9 (2001) 81-83.

[53] H. Nakazawa, S. Miura, R. Kamata, S. Okuno, M. Suemitsu, T. Abe, Appl. Surf. Sci. 264 (2013) 625-632.

[54] H. Nakazawa, S. Miura, R. Kamata, S. Okuno, Y. Enta, M. Suemitsu, T. Abe, Jpn. J. Appl. Phys. 51 (2012) 015603-015603.

[55] I. Bertoti, A. Toth, M. Mohai, J. Szepvölgyi, Surf. Coat. Technol. 206 (2011) 630-639.

[56] E. Dekempeneer, K. VanAcker, K. Vercammen, J. Meneve, D. Neerinck, S. Eufinger, W. Pappaert, M. Sercu, J. Smeets, Surf. Coat. Technol. 142 (2001) 669-673.

[57] C. Chouquet, C. Ducros, S. Barrat, A. Billard, F. Sanchette, Surf. Coat. Technol. 203 (2008) 745-749.

[58] C. Chouquet, J. Gavillet, C. Ducros, F. Sanchette, Mater. Chem. Phys. 123 (2010) 367-371.

[59] M. Klick, Phys. Rev. E 47 (1993) 591-603.

[60] M. Klick, W. Rehak, M. Kammeyer, Jpn. J. Appl. Phys. 36 (1997) 4625-4631.

[61] M. Klick, M. Kammeyer, W. Rehak, W. Kasper, P. Awakowicz, G. Franz, Surf. Coat. Technol. 98 (1998) 1395-1399.

[62] J. Coburn, M. Chen, J. Appl. Phys. 51 (1980) 3134-3136.

[63] V.M. Donnelly, J. Phys. D: Appl. Phys. 37 (2004) 217-236.

[64] X.M. Zhu, Y.K. Pu, J. Phys. D: Appl. Phys. 43 (2010) 403001.

[65] L. Tomasini, A. Rousseau, G. Gousset, P. Leprince, J. Phys. D: Appl. Phys. 29 (1996) 1006-1013.

[66] U. Fantz, Plasma Source Sci. Technol. 15 (2006) 137-147.

[67] C. Biloiu, X. Sun, Z. Harvey,E. Scime, J. Appl. Phys. 101 (2007) 73303-73303.

[68] Y.K. Pu, Y.F. Ren, S.Z. Yang, D. Dywer, X.G. Zhang, X.J. Jia, Surf. Coat. Technol. 131 (2000) 470-473.

[69] G. Crolly, H. Oechsner, Eur. Phys. J. Appl. Phys. 15 (2001) 49-56.

[70] J.B. Boffard, C.C. Lin, C.A. DeJoseph, J. Phys. D: Appl. Phys. 37 (2004) 143-161.

[71] N.A. Sanchez, C. Rincon, G. Zambrano, H. Galindo, P. Prieto, Thin Solid Films 373 (2000) 247-250.

[72] C. Corbella, M. Vives, G. Oncins, C. Canal, J. Andujar, E. Bertran, Diamond Relat. Mater. 13 (2004) 1494-1499.

[73] Th. Welzel, I. Dani, F. Richter, Plasma Source Sci. Technol. 11 (2002) 351-359.

[74] A. Soum-Glaude, L. Thomas, A. Dollet, P. Segur, M.C. Bordage, Diamond Relat. Mater. 16 (2007) 1259-1263.

[75] G. Zambrano, H. Riascos, P. Prieto, E. Restrepo, A. Devia, C. Rincon, Surf. Coat. Technol. 172 (2003) 144-149.

[76] J. Zhou, I.T. Martin, R. Ayers, E. Adams, D. Liu, E.R. Fisher, Plasma Source Sci. Technol. 15 (2006) 714-726.

[77] H. Zhou, J. Watanabe, M. Miyake, A. Ogino, M. Nagatsu, R. Zhan, Diamond Relat. Mater. 16 (2007) 675-678.

[78] D. Rohde, P. Pecher, H. Kersten, W. Jacob, R. Hippler, Surf. Coat. Technol. 149 (2002) 206-216.

[79] A. Keudell, T. Schwarz-Selinger, W. Jacob, Thin Solid Films 308 (1997) 195-198.

[80] S. Ulrich, H. Ehrhardt, J. Schwan, W. Donner, H. Dosch, P. Widmayer, P. Ziemann, Surf. Coat. Technol. 116 (1999) 269-273.

[81] S. Ulrich, J. Ye, M. Stüber, C. Ziebert, Thin Solid Films 518 (2009) 1443-1450.

[82] W.C. Oliver, G.M. Pharr, J. Mater. Res. 7 (1992) 1564-1583.

[83] M.V. Malyshev, V.M. Donnelly, Phys. Rev. E 60 (1999) 6016-6029.

[84] U. Fantz, Plasma Phys. Control. Fusion 40 (1998) 1035-1056.

[85] U. Fantz, Contrib. Plasma Phys. 44 (2004) 508-515.

[86] K. Behringer, Plasma Phys. Control. Fusion 33 (1991) 997-1028.

[87] C.M. Ferreira, J. Loureiro, J. Phys. D: Appl. Phys. 17 (1984) 1175-1188.

[88] R.W.P. McWhirter, in: R.H. Huddlestone, S.L. Leonard (Eds.), Plasma Diagnostic Techniques, Chap. 5, Academic, New York, 1965.

[89] J.E. Chilton, J.B. Boffard, R.S. Schappe, C.C. Lin, Phys. Rev. A 57 (1998) 267-277.

[90] J.E. Chilton, M.D. Stewart Jr., C.C. Lin, Phys. Rev. A 61 (2000) 052708.

[91] J.R. Fuhr, W.L. Wiese, in: D.R. Lide, H.P.R. Frederikse (Eds.), CRC Handbook of Chemistry and Physics, Chap. 10, CRC Press, Boca Raton, Ann Harbor, London, Tokyo, 1994.

[92] K. Behringer, U. Fantz, New J. Phys. 2 (2000) 23.

[93] P. Kurunczi, A. Koharian, K. Becker, K. Martus, Contrib. Plasma Phys. 36 (1996) 723-735.

[94] A.C. Ferrari, J. Robertson, Phys. Rev. B 61 (2000) 14095-14107.

[95] X. Wu, M. Suzuki, T. Ohana, A. Tanaka, Diamond Relat. Mater. 17 (2008) 7-12.